

# Designing electrolyte structure to suppress hydrogen evolution reaction in aqueous batteries

**Qingshun Nian**

Nankai University and University of Science and Technology of China

**Xiaoren Zhang**

Dalian Institute of Chemical Physics

**Yazhi Feng**

Nankai University

**Shuang Liu**

Nankai University

**Tianjiang Sun**

Nankai University

**Xiaodi Ren**

University of Science and Technology of China

**Zhanliang Tao** (✉ [taozhl@nankai.edu.cn](mailto:taozhl@nankai.edu.cn))

Nankai University

**Donghui Zhang**

Dalian Institute of Chemical Physics, Chinese Academy of Sciences <https://orcid.org/0000-0001-9426-8822>

**Jun Chen**

Nankai University <https://orcid.org/0000-0001-8604-9689>

---

## Article

**Keywords:** electrolyte structure, hydrogen evolution reaction (HER), aqueous batteries (ABs), dimethyl sulfoxide (DMSO)

**Posted Date:** November 3rd, 2020

**DOI:** <https://doi.org/10.21203/rs.3.rs-95916/v1>

**License:**  This work is licensed under a Creative Commons Attribution 4.0 International License.

[Read Full License](#)

---

**Version of Record:** A version of this preprint was published at ACS Energy Letters on May 17th, 2021. See the published version at <https://doi.org/10.1021/acsenergylett.1c00833>.

# Designing electrolyte structure to suppress hydrogen evolution reaction in aqueous batteries

Qingshun Nian<sup>1,2</sup>, Xiaoren Zhang<sup>3,4</sup>, Yazhi Feng<sup>1</sup>, Shuang Liu<sup>1</sup>, Tianjiang Sun<sup>1</sup>, Xiaodi Ren<sup>2</sup>✉, Zhanliang Tao<sup>1</sup>✉, Donghui Zhang<sup>3</sup>, Jun Chen<sup>1</sup>

<sup>1</sup>Key Laboratory of Advanced Energy Chemistry (Ministry of Education), College of Chemistry, Nankai University, Tianjin 300071, China.

<sup>2</sup>Hefei National Laboratory for Physical Science at the Microscale. CAS Key Laboratory of Materials for Energy Conversion. Department of Materials Science and Engineering, University of Science and Technology of China, Anhui 230026, China.

<sup>3</sup>State Key Laboratory of Molecular Reaction Dynamics, Dalian Institute of Chemical Physics, Chinese Academy of Sciences, Dalian 116023, China.

<sup>4</sup>University of Chinese Academy of Sciences, Beijing 100049, China.

✉E-mail: taozhl@nankai.edu.cn; xdren@ustc.edu.cn

These authors contributed equally: Qingshun Nian, Xiaoren Zhang.

**Abstract:** Aqueous batteries (ABs) have attracted increasing attention because of their inherent safety and low cost. Nevertheless, hydrogen evolution reaction (HER) at the anode presents severe challenges for stable and safe operation of ABs. Instead of passivating the anode surface to hinder HER kinetics, a novel design strategy is proposed here to suppress the HER via alternating its thermodynamics pathway. By adding a hydrogen bond acceptor, dimethyl sulfoxide (DMSO), the onset potential of HER can be delayed by as much as 1.0 V (on titanium mesh). Spectral characterization and molecular dynamics simulation confirm that the formation of hydrogen bonds between DMSO and water molecules can reduce the water activity, thereby suppressing the HER. This strategy has proven to be universal in expanding the electrochemical window of aqueous electrolytes. For instance, unconventional  $V^{2+} \leftrightarrow V^{3+}$  redox processes in  $Na_3V_2(PO_4)_3$  (-1.2 V *versus* Ag/AgCl) and highly stable Zn plating/stripping processes can be realized in ABs.

**Introduction.** With the ever-increasing demand for large-scale energy storage systems, aqueous rechargeable batteries are receiving unprecedented attentions owing to their advantages of environmental friendliness, non-flammability, low-cost and high ionic conductivity of electrolytes<sup>1-5</sup>. However, traditional aqueous electrolytes provide a narrow electrochemical stability window (1.23 V) limited by the hydrogen evolution reaction (HER) and oxygen evolution reaction (OER)<sup>6-8</sup>. Compared to the OER process, HER presents even more severe challenges due to its high thermodynamic redox potential above most anode materials and its favorable reaction kinetics (two-electron process vs. four-electron process in OER). As a result, Anode materials are refrained from accessing multi-electron reaction processes or suffer from serious side reactions in aqueous electrolytes. Even in trace amounts, hydrogen will severely deteriorate the electrode stability during cycling<sup>9</sup>, which greatly restricts the choice of anode materials for aqueous batteries.

Up to now, several strategies have been implemented in suppressing HER. A common practice was to increase the pH of the electrolyte to lower the HER potential<sup>10,11</sup>. However, strong alkaline solution can influence the stability of most electrode materials. Recently, a “water-in-salt” (WIS) electrolyte (e.g. 21 m lithium bis(trifluoromethane)sulfonimide (21 m LiTFSI))<sup>9</sup> was used in aqueous batteries. By decreasing the amount of free water molecules and forming a solid–electrolyte interphase (SEI) via anion

reduction on the anode, which kinetically prevents sustained reduction of both water and anion, the electrochemical stability of the aqueous electrolyte was improved. However, the onset potential for HER was only reduced by 0.2 V compared to the low-concentration electrolyte (1 m LiTFSI in H<sub>2</sub>O). Although high concentration aqueous electrolytes with different salt species (e.g. nitrate, perchlorate, chloride, acetate and etc.) have been studied<sup>14-19</sup>, their inhibitory effects on HER are not satisfactory. Besides, the suppression of HER in those systems typically relies on the formation of a surface passivation layer, which prevents on the direct contact between the anode and the aqueous electrolyte and avoid excessive water reduction reactions kinetically. Not only extensive optimization of electrolyte formulations is needed to form an effective passivation layer on the anode, but also the passivation layer itself can break to expose new anode-electrolyte interfaces due to anode volume changes in charge/discharge cycles. Besides, using highly concentrated salts (including some highly fluorinated salts, e.g. LiTFSI, lithium bis(pentafluoroethanesulfonyl)imide (LiBETI)<sup>12</sup>, lithiumtri-fluoromethane sulfolate (LiOTF)<sup>13</sup>), may significantly increase the toxicity and cost of electrolyte, which compromises the economic benefits, and plagues the large-scale application of ABs. There are also other strategies to suppress HER, including the current collector design<sup>20</sup>, anode surface protection<sup>21</sup>, molecular crowding electrolytes<sup>22</sup>, etc. Although some excellent results

have been achieved via these strategies, the strict experimental conditions and high-cost hinder the large-scale applications. Taking account of the pitfalls of strategies mentioned, a simple yet universal strategy to decrease the inherent activity of H<sub>2</sub>O in HER is highly desirable.

Here, a novel strategy from the perspective of thermodynamics is firstly introduced to reduce the HER potential of ABs, by manipulating the hydrogen bond (H-bond) structure of water molecules. It was found out that by adding DMSO with a mole fraction of 0.5 into aqueous electrolytes (e.g. 2 m NaClO<sub>4</sub> in H<sub>2</sub>O), the HER potential can be reduced by 1.0 V (from 0.6 V to 1.6 V, *versus* Ag/AgCl with saturated KCl). Spectral characterization and molecular dynamics simulation (MD) demonstrate that all the hydrogen atoms in water molecules are bound in the DMSO-H<sub>2</sub>O H-bond network, which effectively reduces the activity of water molecular. In addition, DMSO enter the cation solvation sheath directly to replace part of coordinating water molecules, thus inhibiting their involvement in interfacial electrochemical reactions. Benefiting from the greatly suppressed HER in aqueous electrolytes via this strategy, efficient utilization of the V<sup>2+</sup>↔V<sup>3+</sup> reaction of the Na<sub>3</sub>V<sub>2</sub>(PO<sub>4</sub>)<sub>3</sub> anode material, which cannot proceed in conventional aqueous electrolytes, can be achieved; in addition, the Coulombic efficiency of Zn metal anode can be largely improved.

## Results

**Electrolyte structure design.** Fig. 1a displays the schematic of HER in aqueous electrolytes. During the charging and discharging process, water molecules migrate to the electrode surface together with cations, and subsequently undergo a deprotonation process to generate hydrogen. This deprotonation step not only changes the chemical bond in water molecules, but also disrupts the intermolecular H-bond. Therefore, HER of water molecules is a competitive process with the H-bond formation process in the solution<sup>22-25,46</sup>. In principle, modulating the H-bond structure of water can reduce the activity of water, thus suppressing HER in ABs.

DMSO, as a highly polar aprotic solvent, can form strong H-bonds with water molecules and significantly change the original H-bond structure of water molecules<sup>26,27</sup>. As shown in Fig. 1b, there are two main types of H-bonds between water molecule and DMSO (1DMSO-2H<sub>2</sub>O, 2DMSO-1H<sub>2</sub>O). Thus, the unique characteristic makes DMSO a favorable H-bond acceptor to form H-bonds with water molecules and reduce their activities. An apparent exothermal reaction was noticed when mixing H<sub>2</sub>O with DMSO, as illustrated by the thermal images of the reaction mixture in Fig. 1c, in which the temperature of the mixed systems rose above 40°C. It was confirmed by Fourier transform infrared spectroscopy (FT-IR, Supplementary Fig. 1) that no new substance is produced when DMSO and water are mixed. Therefore, the heat generated by the mixture should be

attributed to the formation of H-bonds between H<sub>2</sub>O and DMSO molecules. The HER potentials for these aqueous electrolytes (2 m NaClO<sub>4</sub> electrolyte with different mole fractions of DMSO) were evaluated with linear sweep voltammetry (LSV) on platinum electrodes (1 cm × 1 cm), with first cathodic scan curves shown in Fig. 1d. As the amount of DMSO increases, the hydrogen evolution potential decreases. When the DMSO molar fraction is 0.5 (2 m-0.5), the lowest hydrogen evolution potential is obtained, which pushes well beyond the electrochemical equilibrium potential of water. No additional DMSO was added to maintain a relatively low electrochemical impedance of the electrolyte (Supplementary Fig. 2). It is worth mentioning that the strategy for suppressing HER is universal, unlike WIS electrolytes which depend on the selections of suitable salts and their concentrations. The hydrogen evolution potential of 1 m LiTFSI-0.5 (adding DMSO with a mole fraction of 0.5 to 1 m LiTFSI aqueous electrolyte) is lower than that of both 1 m LiTFSI and 21 m LiTFSI (Fig. 1e). Similarly, a low hydrogen evolution potential is achieved after adding DMSO with a mole fraction of 0.5 to 1 m KNO<sub>3</sub> (1 m KNO<sub>3</sub>-0.5) (Supplementary Fig. 3). This result demonstrates that the presence of DMSO in aqueous electrolyte successfully suppressed the HER.

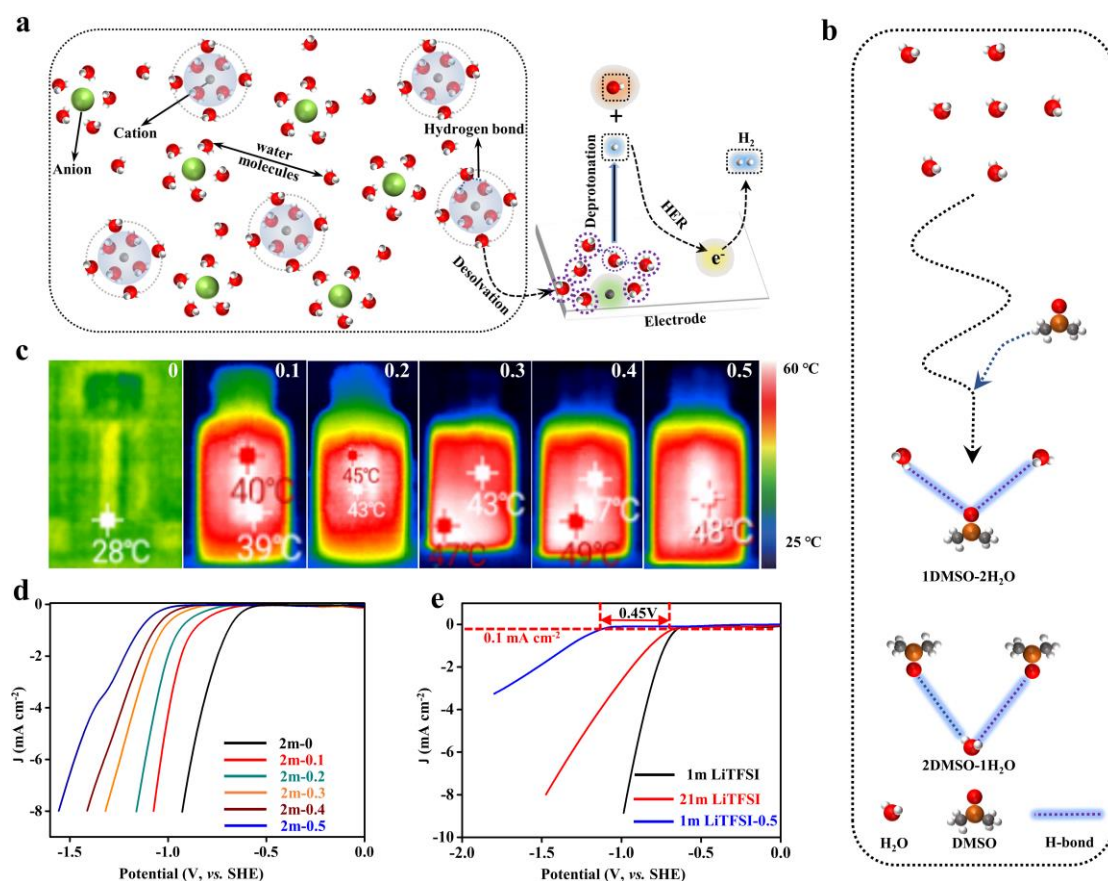


**Fig. 1 The schematic of the electrolyte structure design.** **a** Schematic diagram of the HER process. **b** H-bond patterns between DMSO and water molecules. **c** Thermal imaging pictures when different mole fractions of DMSO and water are mixed (Different areas may have different temperatures). **d** Linear voltammograms recorded at  $10 \text{ mVs}^{-1}$  in 2 m  $\text{NaClO}_4$ -(0~0.5) electrolytes. **e** Linear voltammograms recorded at  $10 \text{ mVs}^{-1}$  in 1 m LiTFSI, 21 m LiTFSI and 1 m LiTFSI-0.5 aqueous electrolytes. We selected the onset potentials at which a current of  $0.1 \text{ mA cm}^{-2}$  is observed to define the hydrogen evolution potential.

### Experimental and theoretical consideration of electrolyte working

**mechanism.** The  $^{23}\text{Na}$  nuclear magnetic resonance (NMR) was utilized as a sensitive indicator to study the surrounding environment of  $\text{Na}^+$ . As shown in Fig. 2a, apparent differences of  $^{23}\text{Na}$  chemical shifts in 2 m-0 and 2 m-0.5 systems were observed, which indicates the  $\text{Na}^+$  solvation structure was changed with the addition of DMSO. Moreover, MD simulation and quantum chemical calculation are applied to deeply understand the

mechanism underlying the H<sub>2</sub>O-DMSO electrolyte systems. While the distribution radii for H<sub>2</sub>O and DMSO within the primary and secondary sheath are the same as that of H<sub>2</sub>O in 2 m-0 system from the radial distribution function (RDF) analysis, the formation of H<sub>2</sub>O-DMSO H-bonds and the changes of relative ratios of H<sub>2</sub>O in solvation sheathes play significant roles in DMSO-induced property alterations. The formation of H-bonds can be evidenced by FT-IR and Raman spectroscopies. Fig. 2c shows the regional FT-IR spectroscopy of 2 m NaClO<sub>4</sub> with different DMSO molar fractions (full FT-IR spectroscopy displayed in Supplementary Fig. 4). As the amount of water molecule increases, the signal of the stretching mode of sulfoxide bond ( $\nu_{S=O}$ , 900-1050 cm<sup>-1</sup>) in FT-IR spectra shifts to a lower wavenumber (Fig. 2ci). Such trend could be explained by the H-bond interaction between the O-H bond in the water molecule and the S=O double bond in DMSO, i.e. S=O····H-O<sup>45</sup>. The two O-H stretching vibration ( $\nu_{O-H}$ ) peaks shift in opposite directions as the DMSO concentration increases (Fig. 2cii). The part that moves to a higher wavenumber is attributed to the vibration of O-H that does not form H-bond with DMSO, and the part that moves to the lower wavenumber is explained by the vibration of O-H that forms H-bond with DMSO<sup>47</sup>. Supplementary Fig. 5 summarizes the Raman spectroscopy of 2 m NaClO<sub>4</sub> with different DMSO molar fractions. Changes of the corresponding peaks in Raman spectroscopy are in consistent with those from the FT-IR

spectroscopy. With more water molecules trapped by DMSO in the H-bond network, the HER suppression would be easier to be observed. We performed statistical analysis for H-bond formation of water with DMSO in different solvation regions to get further details. In 2 m-0.5 system, the averaged H<sub>2</sub>O-DMSO H-bond number distribution in Na<sup>+</sup> solvation sheath is presented in Supplementary Fig. 6. The water molecules replaced by DMSO are distributed in the outer sheath region and formed stable H-bond with outer sheath DMSO as a rather narrowed distribution region has been observed. For those water molecules that participated in H<sub>2</sub>O-DMSO H-bond formation, each of them donates at least one proton in the reaction. We further studied the ratio distribution of 1DMSO-2H<sub>2</sub>O divided by 2DMSO-1H<sub>2</sub>O in different sheath. It is interesting to notice that, in the secondary and outer solvation sheath, over one third of H<sub>2</sub>O-DMSO H-bond adducts are in the form of 1DMSO-2H<sub>2</sub>O (Fig. 2d). Such result indicates that relatively more water would be fixed with H<sub>2</sub>O-DMSO interaction especially for the outer sheath region in which the replacement water is re-distributed. The trapping effects together with the obvious potential reduction of H<sub>2</sub>O-DMSO adduct help to further explain the successful suppression of HER with the addition of DMSO in aqueous electrolyte. Furthermore, we analyzed the coordination number of water and DMSO within each solvation sheath around Na<sup>+</sup> along the simulation trajectories. It is unsurprising to find that, DMSO has penetrated into each

sheath as the averaged number of water is reduced from 6 to 2 in the primary sheath and from 18 to 9 in the secondary sheath, respectively. The replacement has been made with 3 DMSO in primary sheath and 6 DMSO in secondary sheath (Fig. 2e, Supplementary Figs. 7, 8 and 9). Carrying lesser water molecules in  $\text{Na}^+$  solvation sheath would also be beneficial for HER suppression. In order to gain further insights into the mechanism of HER suppression in  $\text{H}_2\text{O}$ -DMSO electrolytes, potentials of  $\text{H}_2$  evolution in water-water and  $\text{H}_2\text{O}$ -DMSO adduct was compared by density functional theory (DFT) calculations. The theoretical potential of  $\text{H}_2$  evolution in  $\text{H}_2\text{O}$ -DMSO adduct (2 m-0.5) is estimated to be reduced by 0.45 V at room temperature (298.15 K) compared with that for water-water adduct, corresponding to a free energy change of  $10.47 \text{ kcal mol}^{-1}$  ( $43.8 \text{ kJ mol}^{-1}$ ) in the  $\text{H}_2\text{O}$ -DMSO adduct from the water-water adduct (Fig. 2f). This further supports our conclusion that the thermodynamic pathway of HER can be effectively modulated by the H-bond network with DMSO addition.

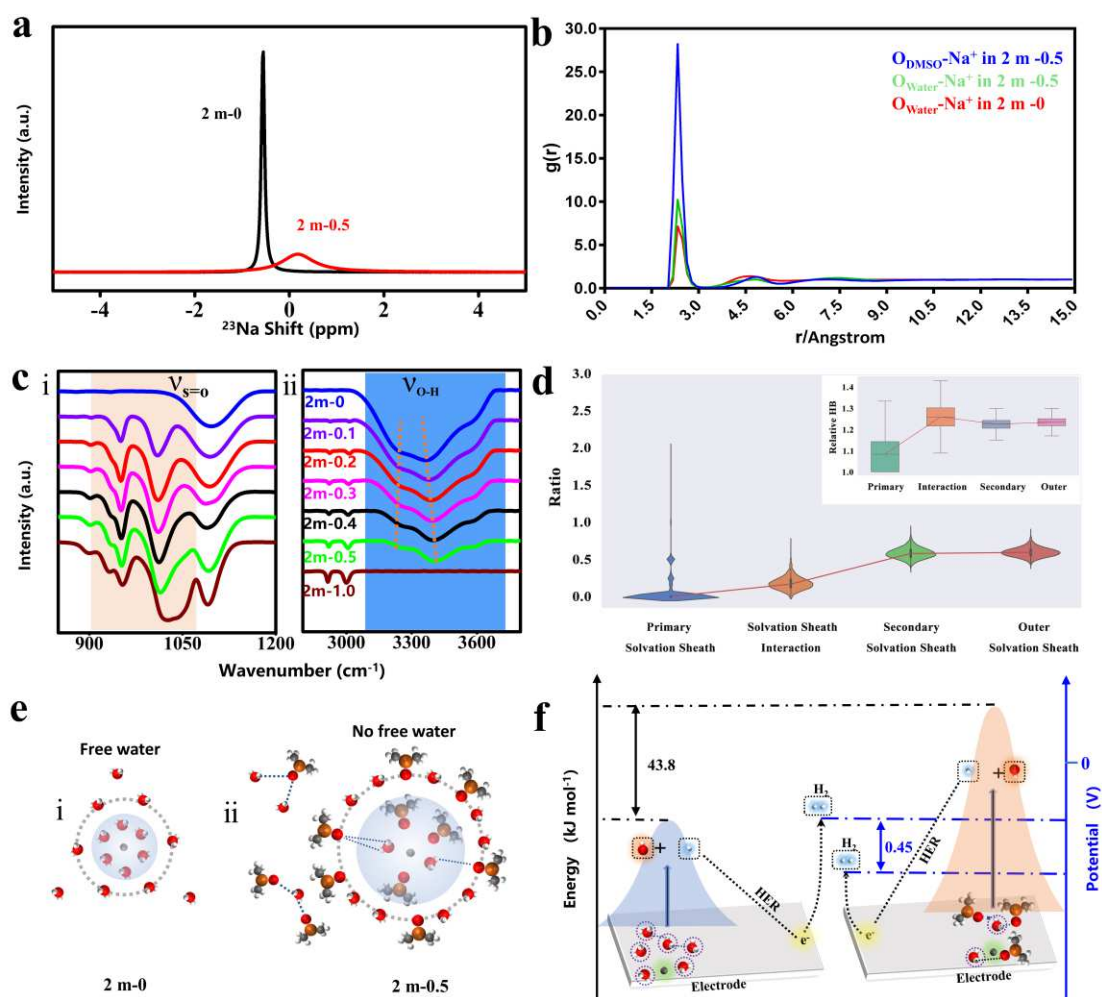


**Fig. 2** The electrolyte structures including H-bonds and  $\text{Na}^+$  solvation structure. **a** The  $^{23}\text{Na}$  NMR spectra in 2 m-0.5 and 2 m-0 electrolytes. **b** The radial distribution function of water and DMSO molecules around  $\text{Na}^+$  in 2 m-0.5 and 2 m-0 systems. The first and second minimum from the center is taken to be the  $\text{Na}^+$  first and second sheath radii. **c** FT-IR of 2 m  $\text{NaClO}_4$  with different mole fractions of DMSO (i) S=O band; (ii) O-H stretching band of water. **d** The statistics of H-bonds formed between water and DMSO in sheath regions (Ratio value, which takes the amount of DMSO molecules in the 1DMSO-2H $_2$ O formation as divisor and the 2DMSO-1H $_2$ O formation as dividend). The inner box-plot counts on the relative HB number in  $\text{Na}^+$  primary sheath (Primary), primary and secondary sheath interaction surface (Interaction), secondary sheath (Secondary) and outer sheath (Outer). The relative H-bond number was calculated as the total H-bond number formed between water and DMSO in each region divided by the number of water molecules participated in the H-bond formation. The outer violin-plot summarizes the ratio distribution of 1DMSO-2H $_2$ O H-bond formation with 2DMSO-1H $_2$ O H-bond formation in each region. The red lines in box-plot and violin-plot are trend indication plotted by the median of each region. **e** The schematic of  $\text{Na}^+$  solvation sheath of (i) 2 m-0 and (ii) 2 m-0.5 systems. **f** The HER potential and energy difference in water-water adduct and H $_2$ O-DMSO adduct.

**Electrochemical performance test.** The overall electrochemical stability window of 2 m-0.5 is expanded to 3.1 V when using titanium meshes as the negative and positive current collectors (Fig. 3a). Particularly, the HER onset potential is pushed from -0.6 V<sup>9</sup> to -1.6 V *versus* Ag/AgCl. A low hydrogen evolution potential can well satisfy reactions that cannot occur in traditional aqueous electrolytes. For example, although Na<sub>3</sub>V<sub>2</sub>(PO<sub>4</sub>)<sub>3</sub> (NVP) can undergo multivalent state transitions (V<sup>2+</sup>↔V<sup>3+</sup>↔V<sup>4+</sup>) (Fig. 3b), the V<sup>2+</sup>↔V<sup>3+</sup> redox process was excluded in traditional aqueous electrolyte systems, because its reaction potential (-1.2 V *versus* Ag/AgCl) is much lower than the HER potential on NVP (-0.8 V *versus* Ag/AgCl in 2 m NaClO<sub>4</sub>). Nevertheless, NVP-based electrode can undergo a highly reversible V<sup>2+</sup>↔V<sup>3+</sup> reaction in the 2 m-0.5 electrolyte (Fig. 3c). The discharge capacity of NVP reaches as high as 180 mAhg<sup>-1</sup> at current density of 0.5 Ag<sup>-1</sup> in the 2 m-0.5 electrolyte (Fig. 3d). To the best of our knowledge, this is the first time that NVP achieves its maximum discharge capacity in an aqueous electrolyte. Fig. 3e presents the cyclic voltammetry (CV) curves of NVP in the 2 m-0.5 system, where two pairs of redox peaks are displayed within the range of -1.4-1.0 V *versus* Ag/AgCl (at a sweep rate of 0.1 mVs<sup>-1</sup>). The voltage difference between the two pairs of redox peaks is 1.7 V. Therefore, a symmetrical battery based on NVP as cathode and anode in 2 m-0.5 can be assembled, as shown schematically in Fig. 3f. The galvanostatic charge-discharge profiles of this symmetrical battery are

illustrated in Fig. 3g. Owing to the greatly improved stability of the electrolyte against HER, the battery achieves an output voltage of 1.7 V and delivers a reversible discharge capacity of  $\sim 90 \text{ mAhg}^{-1}$  (at  $1 \text{ A g}^{-1}$ , based on the total mass of anode and cathode active materials) and a capacity retention of  $\sim 88\%$  after 100 cycles (Fig. 3h).

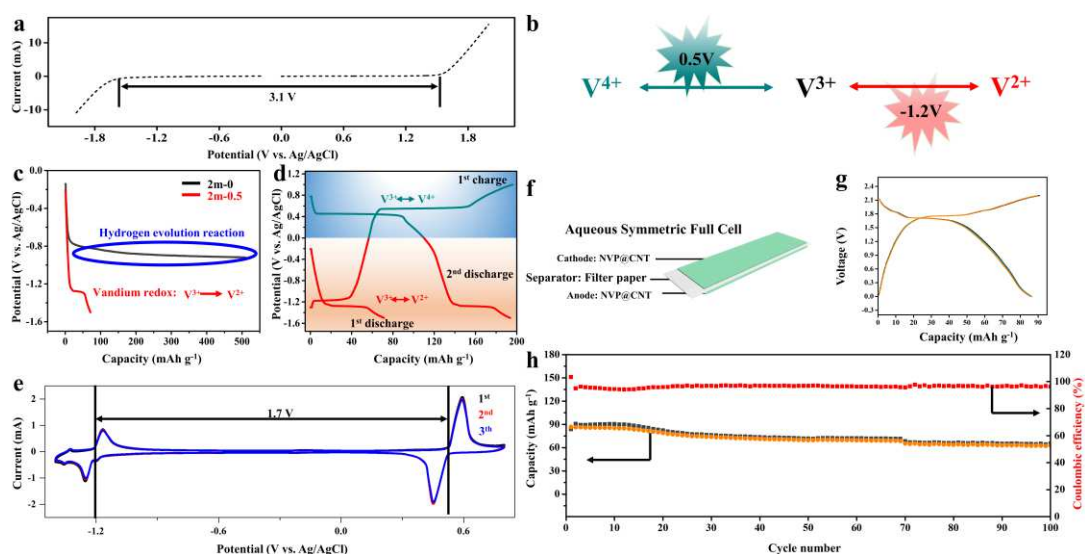


**Fig.3 The electrochemical performance of the NVP anode in the 2 m-0.5 electrolyte.** **a** The electrochemical stability window of 2 m-0.5 on nonactive electrodes. **b** Schematic diagram of  $\text{V}^{2+} \leftrightarrow \text{V}^{3+} \leftrightarrow \text{V}^{4+}$  reaction potential (*versus* Ag/AgCl). **c** Discharge curve of NVP in 2 m-0 (black) and 2 m-0.5 (red). **d** Charge-discharge profiles of NVP in 2 m-0.5. **e** The cyclic voltammetry (CV) curves of NVP at  $0.1 \text{ mV s}^{-1}$  in 2 m-0.5. **f** Schematic diagram of symmetrical battery based on NVP as electrode. **g** The 1<sup>st</sup>, 2<sup>nd</sup>, and 3<sup>th</sup> charge-discharge profiles of NVP symmetrical battery. **h** Cycling performance of NVP symmetrical battery.

To further verify that this methodology is universal in suppressing HER side reactions, its application in aqueous zinc metal batteries (AZMBs) is studied. AZMBs are very attractive energy storage solutions due to their safety, low-cost, etc. Nevertheless, the competitive HER on Zn anode during the charging cycle raises serious challenge to develop AZMBs with high Zn plating/stripping Coulombic efficiencies (CE) and good cycle

stability for practical implementation. In contrast to the clear H<sub>2</sub> evolution and rough Zn plating morphology in the 2 m Zn(CF<sub>3</sub>SO<sub>3</sub>)<sub>2</sub> electrolyte as shown in Fig. 4a-c, a highly smooth Zn surface without H<sub>2</sub> evolution was observed in the 2 m Zn(CF<sub>3</sub>SO<sub>3</sub>)<sub>2</sub>-0.5 electrolyte (2 m Zn(CF<sub>3</sub>SO<sub>3</sub>)<sub>2</sub> added dimethyl sulfoxide (DMSO) with a mole fraction of 0.5) (Fig. 4d-f). More importantly, the average CE of Zn-Ti cell (as calculated from the ratio of Zn removed from the Ti substrate to that of deposited during the same cycle) in the first ten cycles is 99.02% in 2 m Zn(CF<sub>3</sub>SO<sub>3</sub>)<sub>2</sub>-0.5, which remains stable even after 500 cycles (Fig. 4g, h, black line). In contrast, in 2 m Zn(CF<sub>3</sub>SO<sub>3</sub>)<sub>2</sub>, the average CE of the Zn-Ti cell in the first ten cycles is only 85.60% (Fig. 4h, red line) and the CE values fluctuates greatly after ≈13 cycles, which is mainly due to the short circuit of the cell (Fig. 4i). The stability of Zn metal anode was also evaluated by long-term galvanostatic cycling of the symmetric Zn-Zn cells (Fig. 4j). Although with a slightly higher polarization, all cells which use 2 m Zn(CF<sub>3</sub>SO<sub>3</sub>)<sub>2</sub>-0.5 display more stable cycle performance than those using the 2 m Zn(CF<sub>3</sub>SO<sub>3</sub>)<sub>2</sub> electrolyte. After cycling for ~70 h at 1 mA cm<sup>-2</sup>, the polarization voltage drops suddenly in the DMSO-free Zn-Zn cell, which can be ascribed to short circuit induced by Zn dendrite. On the contrary, the Zn-Zn cell using DMSO-containing electrolyte displays a prolonged cycling stability for more than 1600 h. Even at a high rate of 5 mA cm<sup>-2</sup> (0.5 mAh cm<sup>-2</sup> per half cycle) Zn-Zn cells still show excellent cycling stability (Supplementary Fig.

10).

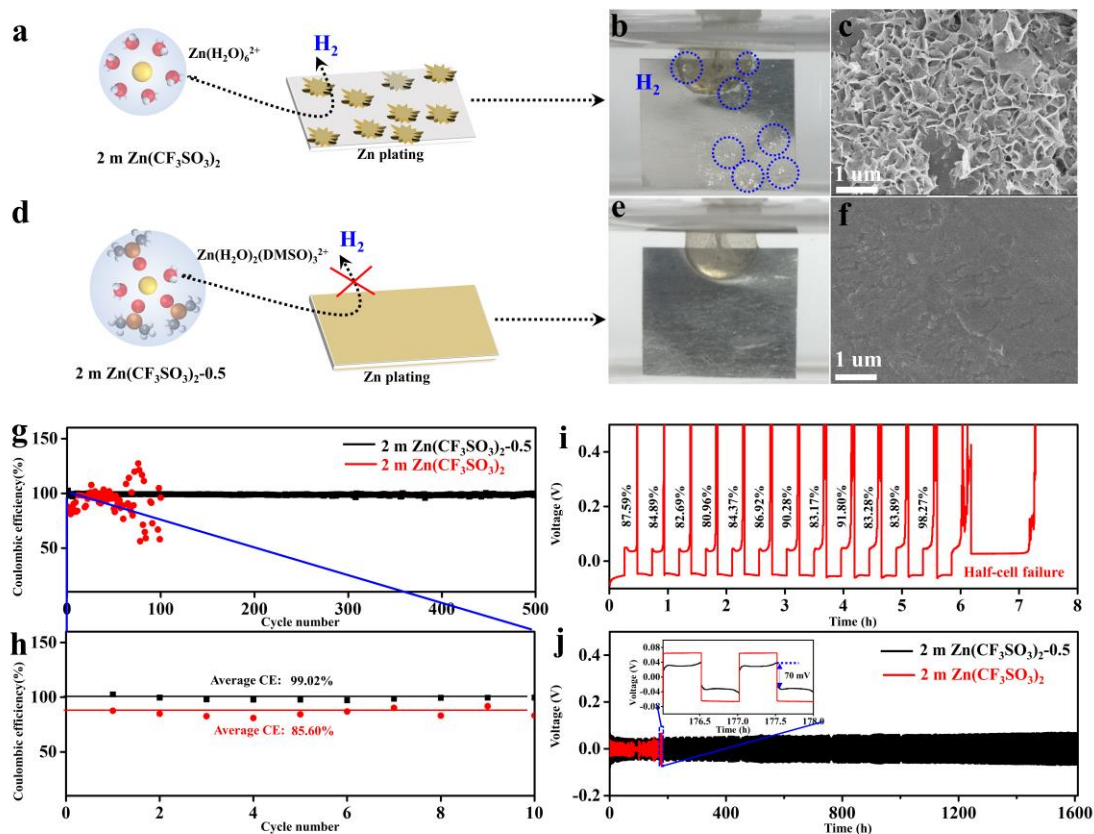


**Fig. 4** The electrochemical performance of the Zn anode. **a**. Schematic diagram of Zn anode behavior with dendrite growth and H<sub>2</sub> evolution in 2 m Zn(CF<sub>3</sub>SO<sub>3</sub>)<sub>2</sub>. **b**. H<sub>2</sub> evolution observed in 2 m Zn(CF<sub>3</sub>SO<sub>3</sub>)<sub>2</sub>. **c** The scanning electron microscopy (SEM) image of Zn deposits using 2 m Zn(CF<sub>3</sub>SO<sub>3</sub>)<sub>2</sub> in Zn-Zn cells at 1 mA cm<sup>-2</sup> (0.5 mAh cm<sup>-2</sup>), after cycling for 100h. **d** Schematic diagram of Zn anode behavior in 2 m Zn(CF<sub>3</sub>SO<sub>3</sub>)<sub>2</sub>-0.5. **e** No H<sub>2</sub> evolution observed in 2 m Zn(CF<sub>3</sub>SO<sub>3</sub>)<sub>2</sub>-0.5. **f** SEM image of Zn deposits using 2 m Zn(CF<sub>3</sub>SO<sub>3</sub>)<sub>2</sub>-0.5 at 1 mA cm<sup>-2</sup> (0.5 mAh cm<sup>-2</sup>), after cycling for 100h. **g**, **h** CE of Zn plating/stripping in different electrolytes obtained from Zn-Ti cells at 1 mA cm<sup>-2</sup> (0.5 mAh cm<sup>-2</sup>). **i** Voltage profiles of Zn plating/stripping using different electrolytes in Zn-Ti cells at a current density of 1 mA cm<sup>-2</sup>. **j** Galvanostatic cycling performance of symmetric Zn-Zn cells tests using different electrolytes at 1 mA cm<sup>-2</sup> (0.5 mAh cm<sup>-2</sup>).

## Discussion

In this work, we demonstrate that the manipulation of intermolecular H-bonds is an effective and universal strategy to suppress the HER side reactions in aqueous electrolytes. DMSO, as a co-solvent, will participate

in the cationic solvation structure, replacing the water molecules in the solvation sheath. At the same time, it can work as a H-bond acceptor to interact with water molecules inside and outside of the solvation sheath. The H-bonds between DMSO and water molecules can confine water molecules through the DMSO-H<sub>2</sub>O H-bond network, thus reducing water activity. The energy barrier for water molecules to deprotonate in the system containing DMSO increases by 43.8 kJ mol<sup>-1</sup>. Benefiting from the suppression of the HER, the electrochemical window of aqueous electrolyte can be greatly expanded, enabling multi-electron redox reactions of NVP with a discharge capacity of 180 mAhg<sup>-1</sup> for the first time (at a current density 0.5 Ag<sup>-1</sup>) and highly stable Zn metal cycling with CEs over 99%. This study provides new insights to suppress the HER of aqueous electrolyte from the perspective of thermodynamics.

## Methods

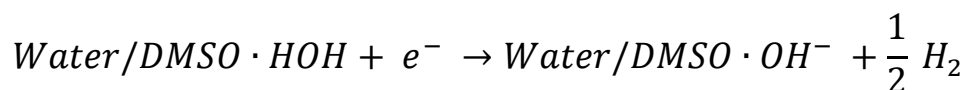
**Preparation of electrolytes and electrodes.** The 2 m-0.5 samples were formed by mixing the two components (2 m NaClO<sub>4</sub> aqueous solution and DMSO) with the required molar ratios (the DMSO/(DMSO+H<sub>2</sub>O) molar ratio is 0.5) at room temperature. The same strategy was used to prepare 2 m Zn(CF<sub>3</sub>SO<sub>3</sub>)<sub>2</sub>-0.5 samples. NVP was synthesized according to the previously reported method<sup>33</sup>. The corresponding characterization of NVP is shown in Supplementary Figs. 11, 12 and 13. The NVP electrodes used here comprise 80 wt% NVP, 10 wt% Super P carbon, and 10 wt% polyvinylidene fluoride (PVDF), which were mixed and dispersed in N-methyl-2-pyrrolidone (NMP) and cast on the Ti current collector (10 μm in thickness). NVP was punched in the diameter of 12 mm (1.1304 cm<sup>2</sup>) for the electrochemistry tests. The active mass loading for the NVP electrode materials was 1.2 ± 1 mg cm<sup>-2</sup> for normal tests. Zn foil (>99.99%) and Ti foil (>99.99%) were purchased from Ailian of Tianjin. Zn and Ti foil were punched in the diameter of 12 mm (1.1304 cm<sup>2</sup>) for the electrochemistry tests.

**Characterization.** Thermal imaging camera (Hti-Xintai HT-101) to record the exothermic phenomenon. NMR spectra were collected on Bruker ASCEND400. FT-IR measurements were carried out on a Perkin-Elmer spectrometer in the transmittance mode. Raman spectroscopy for the electrolyte structure was conducted on Horiba LabRAM HR Evolution

microscope used a 532 nm excitation laser. The scanning electron microscopy (SEM, JEOLJSM-7500F) was employed to detect the morphologies of NVP and Zn deposits on the Zn-metal anodes. The X-ray diffractometer (XRD) patterns were recorded on RigakuMiniFlex600 with Cu-K $\alpha$ 1 radiation ( $\lambda = 1.5405 \text{ \AA}$ ). The high-resolution transmission electron microscopy (HRTEM) was conducted using FEITalosF200XG2.

**Computational methods.** MD simulations were performed on the 2 m NaClO<sub>4</sub> aqueous electrolyte systems with Amber 16 package<sup>34</sup> to deeper understand the solvation shell changes after adding DMSO with 0.5 mole fraction. The force file parameters of ClO<sub>4</sub><sup>-</sup> and DMSO applied here were gathered from the literature<sup>35,36</sup> (Supplementary Table 1). Water molecules were described with TIP3P potential model<sup>37</sup>. A total 100 ns MD production run was performed for each system after minimization run and heating procedure to reach 300 K. The sampling strategies were carried out under NpT condition with 2fs time step. The electrostatic interactions were described with the particle mesh Ewald method (PME)<sup>38</sup> and cutoff threshold of 10  $\text{\AA}$  was applied for non-bonded Van der Waals interaction. The periodic boundary conditions (PBC) and SHAKE algorithm were turned on during the production run<sup>39</sup>. Details of the simulated model components could be referred to Supplementary Table 2. Supplementary Fig. 14 presents the equilibrium properties of the two simulated systems. Analysis was performed based on 10-100ns simulation trajectories.

A quantum chemistry study of the reduction reaction was performed using Gaussian 16 to distinguish the energy profile of H<sub>2</sub> evolution from water in different H-bond systems captured from MD simulations. Density functional B3LYP<sup>40</sup> with 6-311G\* and D3BJ<sup>41</sup> dispersion correction was used for geometrical optimization. The double-hybrid method B2PLYPD3<sup>42</sup> with def2TZVP basis set was applied for thermodynamic correction. The Minnesota functional M052X<sup>43</sup> with equivalent basis set was used to estimate the solvation effects. The SMD solvation model using water solvent parameters was applied in all needed calculation scenarios. The half cycle of H<sub>2</sub> evolution could be described as:



The free energy for the complex of interest denoted as water/DMSO H-bond cluster in solution could be calculated according to the following expression:

$$\begin{aligned} \Delta G^{Sol} &= \Delta G^{Sol}(\text{Water/DMSO} \cdot \text{OH}^-) \\ &\quad - \Delta G^{Sol}(\text{Water/DMSO} \cdot \text{HOH}) \end{aligned}$$

The reduction potential was calculated as:

$$E^0 = -\frac{\Delta G^{Sol}}{F} - SHE$$

Where  $F$  is Faraday's constant (1.0 eV/V) and  $SHE$  is the absolute potential of the standard hydrogen electrode<sup>44</sup>. As we focused on the difference of reduction potential,  $SHE$  part was eliminated from the deduction

calculation, so there is no need for interpretation of the value of *SHE*.

## References

1. Nam, K. W., Park, S. S., Dos Reis, R., Dravid, V. P., Kim, H., Mirkin, C. A. & Stoddart, J. F. Conductive 2D metal-organic framework for high-performance cathodes in aqueous rechargeable zinc batteries. *Nat. Commun.* **10**, 1-10 (2019).
2. Yang, C., Chen, J., Ji, X., Pollard, T. P., Lü, X., Sun, C. J. & Wang, Y. Aqueous Li-ion battery enabled by halogen conversion–intercalation chemistry in graphite. *Nature* **569**, 245-250 (2019).
3. Suo, L. et al. How solid-electrolyte interphase forms in aqueous electrolytes. *J. Am. Chem. Soc.* **139**, 18670-18680 (2017).
4. Gao, H. & Goodenough, J. B. An Aqueous symmetric sodium-ion battery with NASICON-structured  $\text{Na}_3\text{MnTi}(\text{PO}_4)_3$ . *Angew. Chem. Int. Ed.* **128**, 12960-12964 (2016).
5. Guo, Z., Zhao, Y., Ding, Y., Dong, X., Chen, L., Cao, J. & Wang, Y. Multi-functional flexible aqueous sodium-ion batteries with high safety. *Chem* **3**, 348-362 (2017).
6. Eftekhari, A. High-energy aqueous lithium batteries. *Adv. Energy Mater.* **8**, 1801156 (2018).
7. Liu, Z., Huang, Y., Huang, Y., Yang, Q., Li, X., Huang, Z. & Zhi, C. Voltage issue of aqueous rechargeable metal-ion batteries. *Chem. Soc. Rev.* **49**, 180-232 (2020).

8. Chao, D. & Qiao, S. Z. Toward high-voltage aqueous batteries: super- or low-concentrated electrolyte? *Joule* **4**, 1846-1851 (2020).
9. Suo, L., Borodin, O., Gao, T., Olguin, M., Ho, J., Fan, X. & Xu, K. “Water-in-salt” electrolyte enables high-voltage aqueous lithium-ion chemistries. *Science* **350**, 938-943 (2015).
10. Li, W., McKinnon, W. R. & Dahn, J. R. Lithium intercalation from aqueous solutions. *J. Electrochem. Soc.* **141**, 2310 (1994).
11. Luo, J. Y., Cui, W. J., He, P. & Xia, Y. Y. Raising the cycling stability of aqueous lithium-ion batteries by eliminating oxygen in the electrolyte. *Nat. Chem.* **2**, 760-765 (2010).
12. Yamada, Y., Usui, K., Sodeyama, K., Ko, S., Tateyama, Y. & Yamada, A. Hydrate-melt electrolytes for high-energy-density aqueous batteries. *Nat. Energy* **1**, 1-9 (2016).
13. Suo, L., Borodin, O., Sun, W., Fan, X., Yang, C., Wang, F. & Russell, S. M. Advanced high-voltage aqueous lithium-ion battery enabled by “water-in-bisalt” electrolyte. *Angew. Chem. Int. Ed.* **128**, 7252-7257 (2016).
14. Zheng, J., Tan, G., Shan, P., Liu, T., Hu, J., Feng, Y. & Lu, J. Understanding thermodynamic and kinetic contributions in expanding the stability window of aqueous electrolytes. *Chem* **4**, 2872-2882 (2018).
15. Lee, M. H., Kim, S. J., Chang, D., Kim, J., Moon, S., Oh, K. & Lee, B.

- Toward a low-cost high-voltage sodium aqueous rechargeable battery. *Mater. Today* **29**, 26-36 (2019).
16. Zhang, L., Rodríguez-Pérez, I. A., Jiang, H., Zhang, C., Leonard, D. P., Guo, Q. & Ji, X. ZnCl<sub>2</sub> “Water-in-Salt” electrolyte transforms the performance of vanadium oxide as a Zn battery cathode. *Adv. Funct. Mater.* **29**, 1902653 (2019).
17. Lukatskaya, M. R. et al. Concentrated mixed cation acetate “water-in-salt” solutions as green and low-cost high voltage electrolytes for aqueous batteries. *Energy Environ. Sci.* **11**, 2876–2883 (2018).
18. Liu, T., Tang, L., Luo, H., Cheng, S. & Liu, M. A promising water-in-salt electrolyte for aqueous based electrochemical energy storage cells with a wide potential window: highly concentrated HCOOK. *Chem. Commun.* **55**, 12817-12820 (2019).
19. Leonard, D. P., Wei, Z., Chen, G., Du, F. & Ji, X. Water-in-salt electrolyte for potassium-ion batteries. *ACS Energy Lett.* **3**, 373-374 (2018).
20. Hou, Z., Zhang, X., Ao, H., Liu, M., Zhu, Y. & Qian, Y. Passivation effect for current collectors enables high-voltage aqueous sodium ion batteries. *Mater. Today Energy* **14**, 100337 (2019).
21. Wang, H., Tan, R., Yang, Z., Feng, Y., Duan, X., & Ma, J. Stabilization perspective on metal anodes for aqueous batteries. *Adv. Energy Mater.* 2000962 (2020)

- 22.Xie, J., Liang, Z. & Lu, Y. C. Molecular crowding electrolytes for high-voltage aqueous batteries. *Nat. Mater.* 1-6 (2020).
- 23.Yang, W., Du, X., Zhao, J., Chen, Z., Li, J., Xie, J. & Wang, C. Hydrated eutectic electrolytes with ligand-oriented solvation shells for long-cycling zinc-organic batteries. *Joule* **4**, 1557-1574 (2020).
- 24.Barnum, D. W. Hydrolysis of cations. Formation constants and standard free energies of formation of hydroxy complexes. *Inorg. Chem.* **22**, 2297-2305 (1983).
- 25.Gao, M. et al. RNA hairpin folding in the crowded cell. *Angew. Chem. Int. Ed.* **55**, 3224–3228 (2016).
- 26.Nian, Q. et al. Aqueous batteries operated at -50 °C. *Angew. Chem. Int. Ed.* **131**, 17150-17155 (2019).
- 27.Borin, I. A., Skaf, M. S. Molecular association between water and dimethyl sulfoxide in solution: A molecular dynamics simulation study. *J. Chem. Phys.* **110**, 6412-6420 (1999).
- 28.Yang, W., Du, X., Zhao, J., Chen, Z., Li, J., Xie, J. & Wang, C. Hydrated Eutectic Electrolytes with Ligand-Oriented Solvation Shells for Long-Cycling Zinc-Organic Batteries. *Joule* **4**, 1557-1574(2020).
- 29.Zheng, J., Zhao, Q., Tang, T., Yin, J., Quilty, C. D. Renderos, G. D. & Jaye, C. Reversible epitaxial electrodeposition of metals in battery anodes. *Science* **366**, 645-648 (2019).
- 30.Wang, S. B. et al. Lamella-nanostructured eutectic zinc–aluminum

- alloys as reversible and dendrite-free anodes for aqueous rechargeable batteries. *Nat. Commun.* **11**, 1-9 (2020).
31. Wang, F., Borodin, O., Gao, T., Fan, X., Sun, W., Han, F. & Wang, C. Highly reversible zinc metal anode for aqueous batteries. *Nat. Mater.* **17**, 543-549 (2018).
32. Zhao, Z. et al. Long-life and deeply rechargeable aqueous Zn anodes enabled by a multifunctional brightener-inspired interphase. *Energy Environ. Sci.* **12**, 1938-1949 (2019).
33. Wang, C. et al. A High-Power Na<sub>3</sub>V<sub>2</sub>(PO<sub>4</sub>)<sub>3</sub>-Bi Sodium-Ion Full Battery in a Wide Temperature Range. *Adv. Energy Mater.* **9**, 1900022 (2019).
34. Case, D.A. et al. AMBER 16. University of California, San Francisco (2017).
35. Fox, T. & Kollman, P. A. Application of the RESP methodology in the parametrization of organic solvents. *J. Phys. Chem. B*, **102**, 8070-8079 (1998).
36. Baaden, M., Berny, F., Madic, C. & Wipff, G. M<sup>3+</sup> lanthanide cation solvation by acetonitrile: The role of cation size, counterions, and polarization effects investigated by molecular dynamics and quantum mechanical simulations. *J. Phys. Chem. A*, **104**, 7659-7671 (2000).
37. Jorgensen, W. L., Chandrasekhar, J., Madura, J. D., Impey, R. W. & Klein, M. L. Comparison of simple potential functions for simulating

- liquid water. *J. Chem. Phys.* **79**, 926-935 (1983).
38. Essmann, U., Perera, L., Berkowitz, M. L., Darden, T., Lee, H. & Pedersen, L. G. A smooth particle mesh Ewald method. *J. Chem. Phys.* **103**, 8577-8593 (1995).
39. Ryckaert, J. P., Ciccotti, G. & Berendsen, H. J. Numerical integration of the cartesian equations of motion of a system with constraints: molecular dynamics of n-alkanes. *J. Comput. Phys.* **23**, 327-341 (1977).
40. Becke, A. D. Density-functional thermochemistry. III. The role of exact exchange. *J. Chem. Phys.* **98**, 5648 (1993).
41. Grimme, S., Ehrlich, S. & Goerigk, L. Effect of the damping function in dispersion corrected density functional theory. *J. Comput. Chem.* **32**, 1456-1465(2011).
42. Goerigk, L. & Grimme, S. Efficient and Accurate Double-Hybrid-Meta-GGA Density Functionals Evaluation with the Extended GMTKN30 Database for General Main Group Thermochemistry, Kinetics, and Noncovalent Interactions. *J. Chem. Theory Comput.* **7**, 291-309 (2011).
43. Zhao, Y., Schultz, N. E. & Truhlar, D. G. Design of density functionals by combining the method of constraint satisfaction with parametrization for thermochemistry, thermochemical kinetics, and noncovalent interactions. *J. Chem. Theory Comput.* **2**, 364-382 (2006).
44. Marenich, A. V., Ho, J., Coote, M. L., Cramer, C. J. & Truhlar, D. G. Computational electrochemistry: prediction of liquid-phase reduction

- potentials. *Phys. Chem. Chem. Phys.* **16**, 15068-15106 (2014).
45. Bertoluzza, A., Bonora, S., Battaglia, M. A. & Monti, P. Raman and infrared study on the effects of dimethylsulphoxide (DMSO) on water structure. *J. Raman Spectrosc.* **8**, 231-235 (1979).
46. Ferreira, L. A., Uversky, V. N. & Zaslavsky, B. Y. Role of solvent properties of water in crowding effects induced by macromolecular agents and osmolytes. *Mol. Biosyst.* **13**, 2551–2563 (2017).
47. Wallace, V. M., Dhumal, N. R., Zehentbauer, F. M. et al. Revisiting the aqueous solutions of dimethyl sulfoxide by spectroscopy in the mid- and near-infrared: experiments and car-parrinello simulations. *J. Phys. Chem. B* **119**, 14780-14789 (2015).

## **Acknowledgements**

This study was supported by the National Key R&D Program of China (2016YFB0901500, 2017YFA0206702); the National Natural Science Foundation of China (51771094, 21835004, 21905265 and 21773226), Ministry of Education of China (B12015 and IRT13R30), and Tianjin High-Tech (No. 18JCZDJC31500).

## **Author contributions**

Z.T. and J. C. proposed the concept and supervised the work; Q.N. and X.Z. designed and performed the experiments and the calculations; Y.F., S.L. and T.S. performed the cell assembly; X. R. and D. Z. helped to discuss and analyze the data; all authors discussed and revised the manuscript.

## **Competing interests**

The authors declare no competing interests.

# Figures

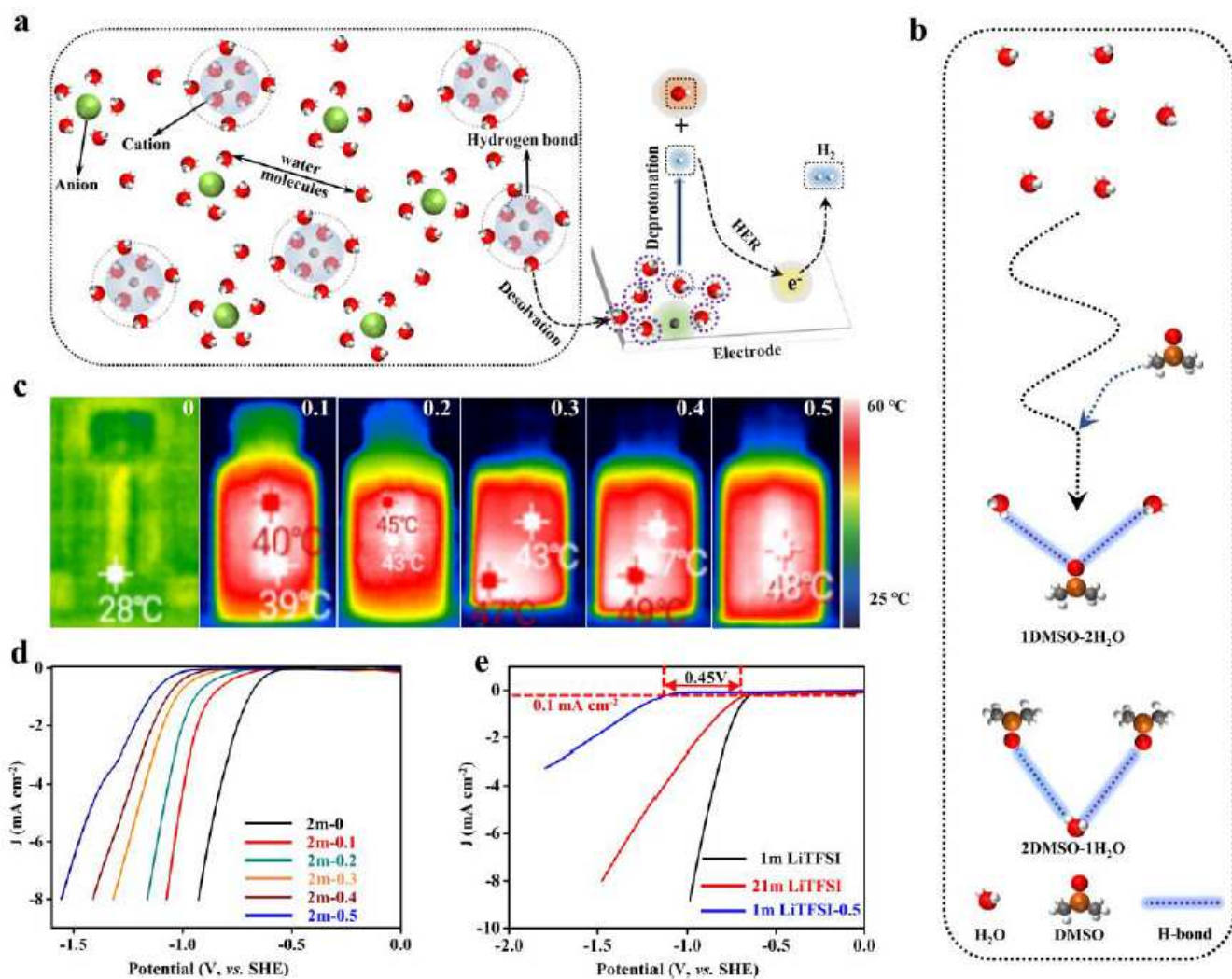


**Figure 1**

The schematic of the electrolyte structure design. **a** Schematic diagram of the HER process. **b** H-bond patterns between DMSO and water molecules. **c** Thermal imaging pictures when different mole fractions of DMSO and water are mixed (Different areas may have different temperatures). **d** Linear voltammetry curves recorded at 10 mVs<sup>-1</sup> in 2 m NaClO<sub>4</sub>-(0~0.5) electrolytes. **e** Linear voltammetry curves recorded at 10 mVs<sup>-1</sup> in 1 m LiTFSI, 21 m LiTFSI and 1 m LiTFSI-0.5 aqueous electrolytes. We selected the onset potentials at which a current of 0.1 mA cm<sup>-2</sup> is observed to define the hydrogen evolution potential.

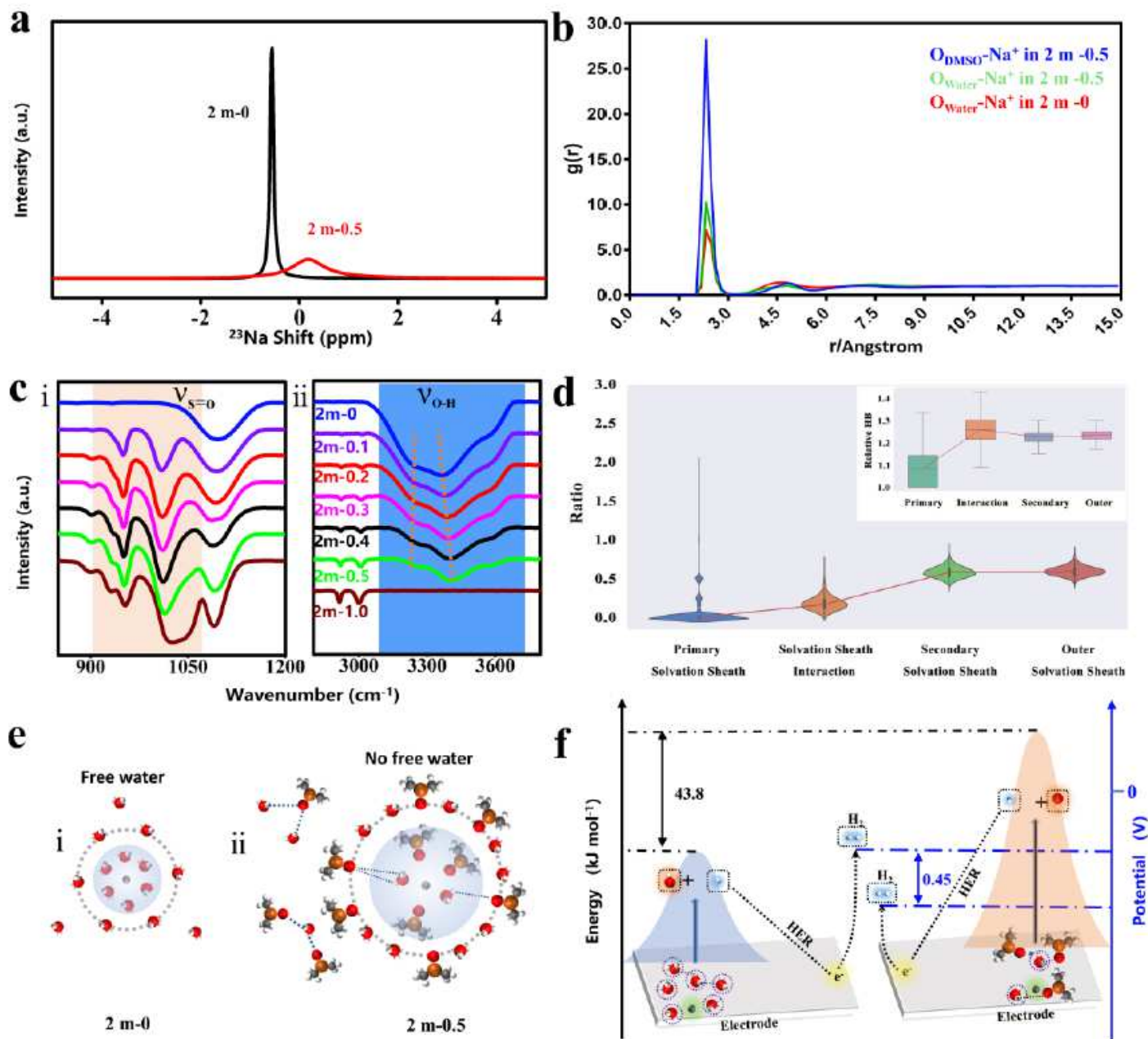


**Figure 2**

The electrolyte structures including H-bonds and  $\text{Na}^+$  solvation structure. a The  $^{23}\text{Na}$  NMR spectra in 2 m-0.5 and 2 m-0 electrolytes. b The radial distribution function of water and DMSO molecules around  $\text{Na}^+$  in 2 m-0.5 and 2 m-0 systems. The first and second minimum from the center is taken to be the  $\text{Na}^+$  first and second sheath radii. c FT-IR of 2 m  $\text{NaClO}_4$  with different mole fractions of DMSO ( $\boxtimes$ ) S=O band; ( $\boxtimes$ ) O-H stretching band of water. d The statistics of H-bonds formed between water and DMSO in sheath regions (Ratio value, which takes the amount of DMSO molecules in the 1DMSO-2H<sub>2</sub>O formation as divisor and the 2DMSO-1H<sub>2</sub>O formation as dividend). The inner box-plot counts on the relative HB number in  $\text{Na}^+$  primary sheath (Primary), primary and secondary sheath interaction surface (Interaction), secondary sheath (Secondary) and outer sheath (Outer). The relative H-bond number was calculated as the total H-bond number formed between water and DMSO in each region divided by the number of water

molecules participated in the H-bond formation. The outer violin-plot summarizes the ratio distribution of 1DMSO-2H<sub>2</sub>O H-bond formation with 2DMSO-1H<sub>2</sub>O H-bond formation in each region. The red lines in box-plot and violin-plot are trend indication plotted by the median of each region. e The schematic of Na<sup>+</sup> solvation sheath of (i) 2 m-0 and (ii) 2 m-0.5 systems. f The HER potential and energy difference in water-water adduct and H<sub>2</sub>O-DMSO adduct.

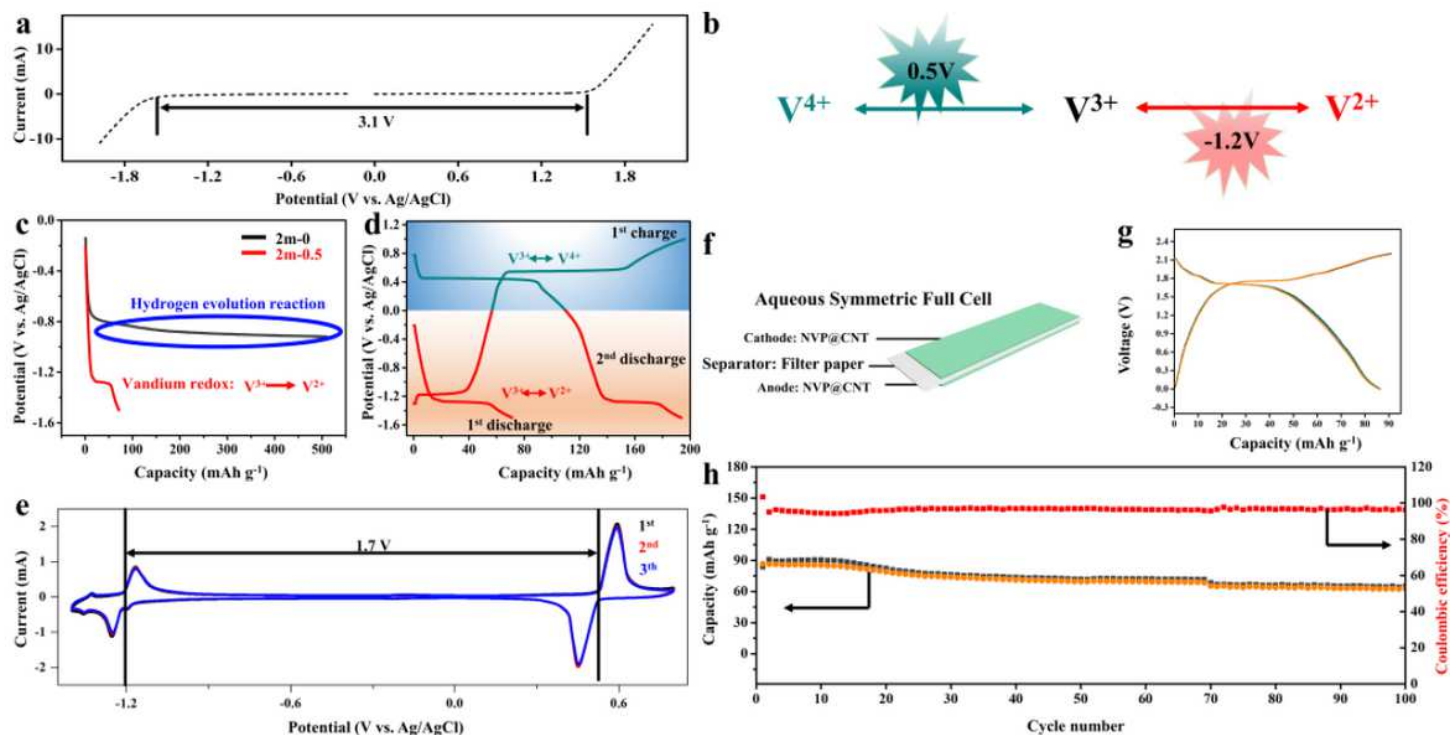


**Figure 3**

The electrochemical performance of the NVP anode in the 2 m-0.5 electrolyte. a The electrochemical stability window of 2 m-0.5 on nonactive electrodes. b Schematic diagram of  $V^{2+} \leftrightarrow V^{3+} \leftrightarrow V^{4+}$  reaction potential (versus Ag/AgCl). c Discharge curve of NVP in 2 m-0 (black) and 2 m-0.5 (red). d Charge-discharge profiles of NVP in 2 m-0.5. e The cyclic voltammety (CV) curves of NVP at 0.1 mV s<sup>-1</sup> in 2 m-0.5. f Schematic diagram of symmetrical battery based on NVP as electrode. g The 1st, 2nd, and 3th charge-discharge profiles of NVP symmetrical battery. h Cycling performance of NVP symmetrical battery.

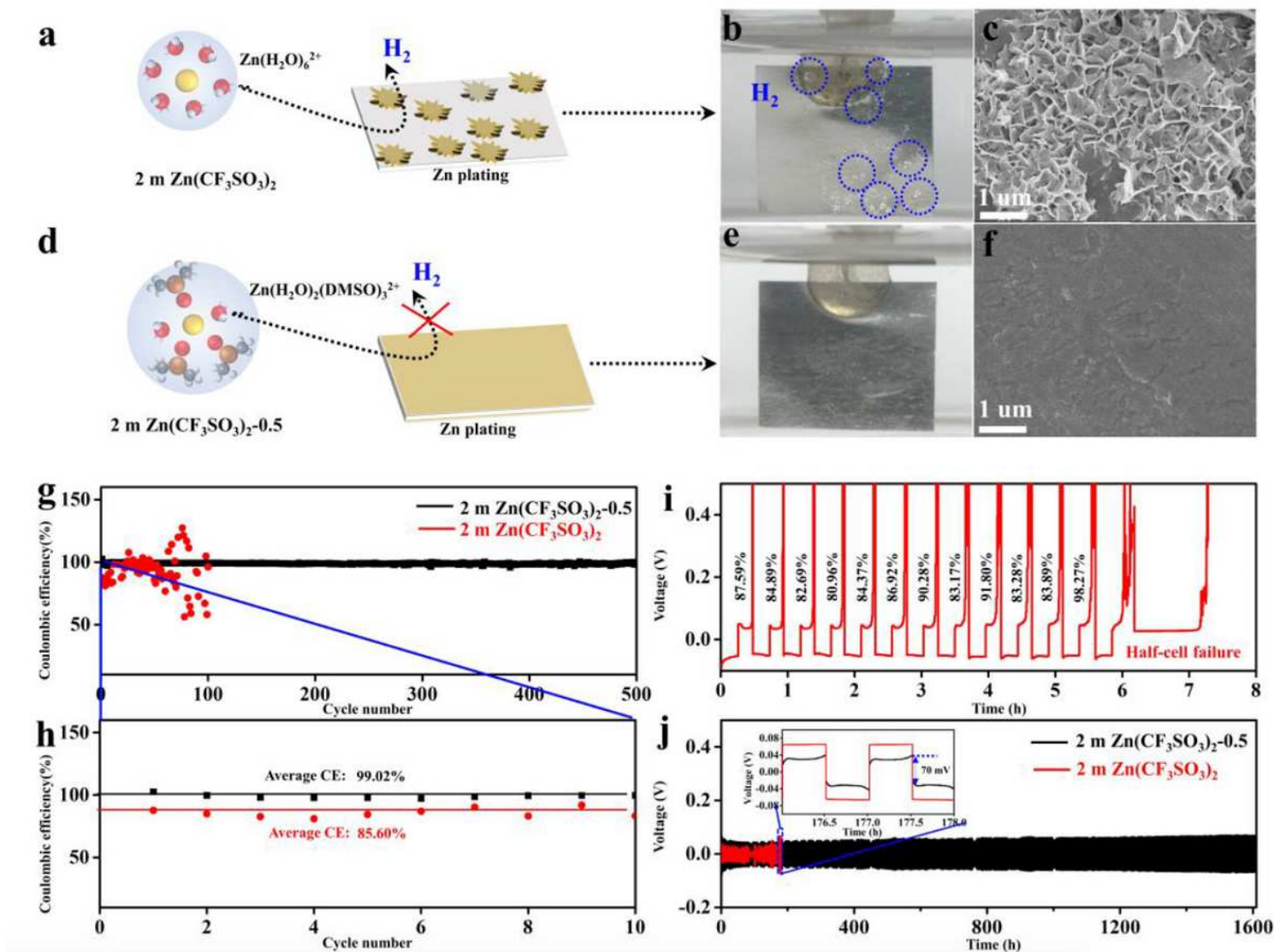


**Figure 4**

The electrochemical performance of the Zn anode. a. Schematic diagram of Zn anode behavior with dendrite growth and  $\text{H}_2$  evolution in 2 m  $\text{Zn}(\text{CF}_3\text{SO}_3)_2$ . b.  $\text{H}_2$  evolution observed in 2 m  $\text{Zn}(\text{CF}_3\text{SO}_3)_2$ . c. The scanning electron microscopy (SEM) image of Zn deposits using 2 m  $\text{Zn}(\text{CF}_3\text{SO}_3)_2$  in Zn-Zn cells at 1 mA  $\text{cm}^{-2}$  (0.5 mAh  $\text{cm}^{-2}$ ), after cycling for 100h. d. Schematic diagram of Zn anode behavior in 2 m  $\text{Zn}(\text{CF}_3\text{SO}_3)_2-0.5$ . e. No  $\text{H}_2$  evolution observed in 2 m  $\text{Zn}(\text{CF}_3\text{SO}_3)_2-0.5$ . f. SEM image of Zn deposits using 2 m  $\text{Zn}(\text{CF}_3\text{SO}_3)_2-0.5$  at 1 mA  $\text{cm}^{-2}$  (0.5 mAh  $\text{cm}^{-2}$ ), after cycling for 100h. g, h CE of Zn plating/stripping in different electrolytes obtained from Zn-Ti cells at 1 mA  $\text{cm}^{-2}$  (0.5 mAh  $\text{cm}^{-2}$ ). i. Voltage profiles of Zn plating/stripping using different electrolytes in Zn-Ti cells at a current density of 1 mA  $\text{cm}^{-2}$ . j. Galvanostatic cycling performance of symmetric Zn-Zn cells tests using different electrolytes at 1 mA  $\text{cm}^{-2}$  (0.5 mAh  $\text{cm}^{-2}$ ).

## Supplementary Files

This is a list of supplementary files associated with this preprint. Click to download.

- [SupplementaryInformation.pdf](#)